nature photonics

ARTICLES

https://doi.org/10.1038/s41566-020-0591-3

Flat optics for image differentiation

You Zhou[1], Hanyu Zheng[2], Ivan I. Kravchenko[3] and Jason Valentine[4]✉

Image processing has become a critical technology in a variety of science and engineering disciplines. Although most image processing is performed digitally, optical analog processing has the advantages of being low-power and high-speed, but it requires a large volume. Here, we demonstrate flat optics for direct image differentiation, allowing us to significantly shrink the required optical system size. We first demonstrate how the differentiator can be combined with traditional imaging systems such as a commercial optical microscope and camera sensor for edge detection with a numerical aperture up to 0.32. We next demonstrate how the entire processing system can be realized as a monolithic compound flat optic by integrating the differentiator with a metalens. The compound nanophotonic system manifests the advantage of thin form factor as well as the ability to implement complex transfer functions, and could open new opportunities in applications such as biological imaging and computer vision.

Imaging processing is a critical and rapidly advancing technology for various science and engineering disciplines, with ever more complex digital tools opening the door to new avenues in biological imaging, three-dimensional (3D) reconstruction and autonomous cars. Edge-based enhancement[1,2] is particularly useful for data compression[3], object inspection[4], microscopy[5–7] and general computer vision[8]. Edge-based enhancement is accomplished using spatial differentiation, which can be based on either electronic or optical architectures. Although digital circuits are able to perform complex data processing, there are limitations due to computation speed and power consumption. Optical analog computation[9], with the ability to process information directly using the optical signal, provides an alternative approach to perform large-scale and real-time data processing with minimal, if any, power consumption.

Traditionally, analog image differentiation has been performed using Fourier methods based on lenses and filter systems. However, the use of multiple conventional lenses, such as those found in 4*f* Fourier filtering, results in a large form factor that is not compatible with compact integrated systems. One option for significantly reducing the optical system size is to employ nanophotonic materials such as metasurfaces[10] and photonic crystals[11] for optical image processing. For example, it has been shown that multiple metasurfaces can be used to perform a range of mathematical operations[12] and there have been several theoretical proposals for image differentiation using single-layer nanophotonic materials[13–15]. Furthermore, image differentiation has been experimentally demonstrated using photonic crystals[16], the spin Hall effect[17], surface plasmon-based devices[18] and the Pancharatnam–Berry phase[19]. However, these past experimental approaches have been restricted to 1D and some require additional refractive elements (prisms or lenses) for either plasmon coupling or performing a Fourier transform, which negates the advantage of the thin and flat elements.

In this work, we experimentally demonstrate a 2D spatial differentiator that operates in transmission. As shown in Fig. 1a,b, the differentiator consists of a Si nanorod photonic crystal that can transform an image, E_{in}, into its second-order derivative, $E_{out} \propto \nabla^2 E_{in}$, allowing for direct discrimination of the edges in the image. The use of a 2D photonic crystal allows for differentiation and edge detection in all directions with a numerical aperture (NA) up to 0.315 and an experimental resolution smaller than 4 μm. The nanophotonic differentiator is directly integrated into an optical microscope and onto a camera sensor, demonstrating the ease with which it can be vertically integrated into existing imaging systems. Furthermore, we demonstrate integration with a metalens for realizing a compact and monolithic image-processing system. In all cases, the use of the nanophotonic differentiator allows for a significant reduction in size compared to traditional systems, opening new doors for optical analog image processing in applications involving computer vision.

Results

To perform second-order spatial differentiation, an optical filter or material should act as a Laplacian operator on the transmitted light with an electric field profile given by $E_{out} \propto \nabla^2 E_{in}$, where ∇^2 is given by $\frac{\partial^2}{\partial x^2} + \frac{\partial^2}{\partial y^2}$. In this case the optical transfer function $H(k_x,k_y)$ follows the function[20]

$$H(k_x,k_y) \equiv \begin{bmatrix} H_{ss}(k_x,k_y) & H_{sp}(k_x,k_y) \\ H_{ps}(k_x,k_y) & H_{pp}(k_x,k_y) \end{bmatrix} = \begin{bmatrix} c_{ss}\left(k_x^2+k_y^2\right) & c_{sp}\left(k_x^2+k_y^2\right) \\ c_{ps}\left(k_x^2+k_y^2\right) & c_{pp}\left(k_x^2+k_y^2\right) \end{bmatrix} \quad (1)$$

where *s*, *p* on the first and second subscript denote the polarization of the incident and transmitted light, respectively, and c_{sp} and c_{ps} correspond to polarization conversion. To achieve the required transfer function we used a photonic crystal slab supporting quasi-guided modes. Unlike modes guided below the light line[21], quasi-guided modes are leaky, propagating in the high-index dielectric slab within the light cone[22,23]. When the frequency, momentum and symmetry match with the quasi-guided modes, Fano interference occurs between the direct transmission and quasi-guided mode, which can lead to near-unity back reflection or transmission[24–26]. In recent experimental work, Fano interference in 1D photonic crystals has been employed for spatial differentiation[16] and theoretical work has been carried out on 2D photonic crystals[15] for this purpose, although the NA was limited. Here, we employ a 2D design

[1]Interdisciplinary Materials Science Program, Vanderbilt University, Nashville, TN, USA. [2]Department of Electric Engineering and Computer Science, Vanderbilt University, Nashville, TN, USA. [3]Center for Nanophase Materials Sciences, Oak Ridge National Laboratory, Oak Ridge, TN, USA. [4]Department of Mechanical Engineering, Vanderbilt University, Nashville, TN, USA. ✉e-mail: jason.g.valentine@vanderbilt.edu

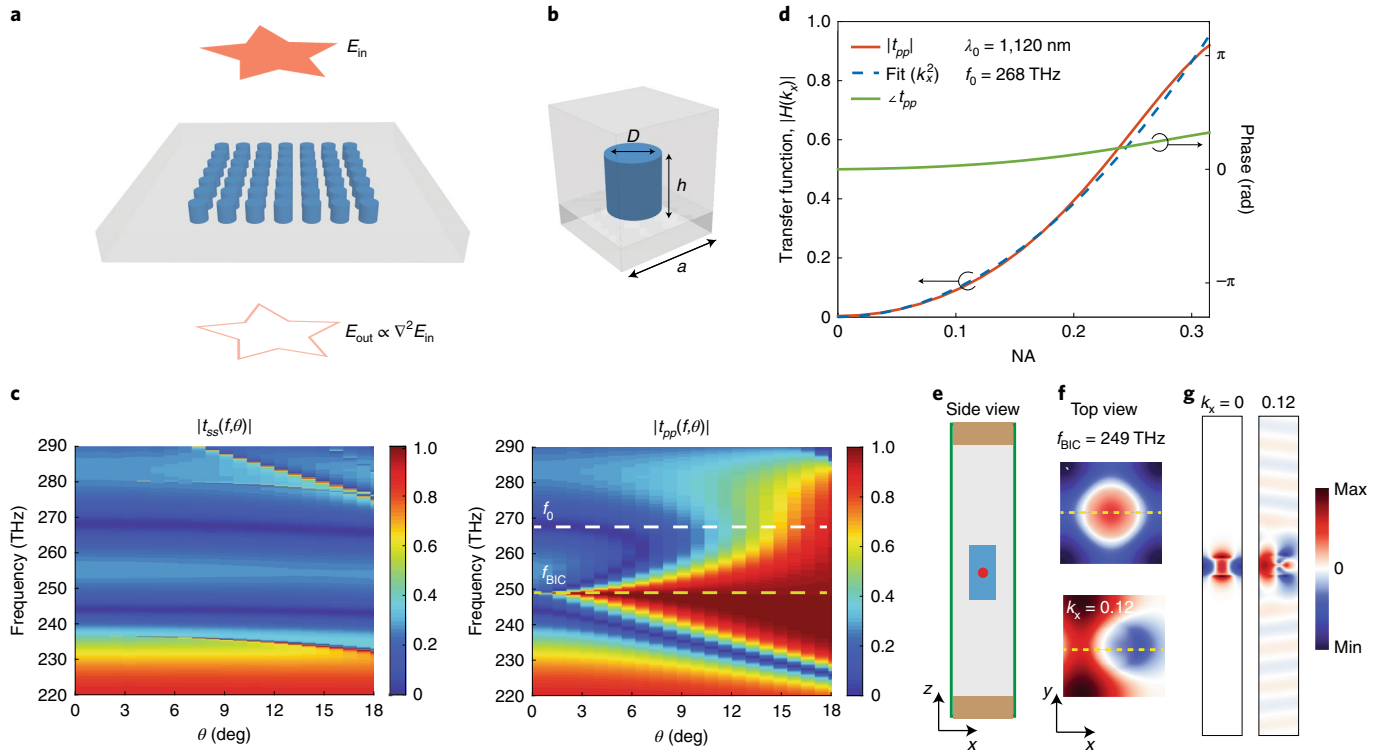

Fig. 1 | Two-dimensional image differentiation using nanophotonic materials. a, Schematic of a photonic crystal slab acting as a Laplacian operator that transforms an image, E_{in}, into its second-order derivative, $E_{out} \propto \nabla^2 E_{in}$. **b**, The unit cell of the differentiator, composed of Si nanorods. **c**, Simulated colour-coded transmission coefficient amplitude $|t(f,\theta)|$ as a function of frequency and incident angle along the Γ–X direction ($\varphi = 0°$) for *s* and *p* polarization. **d**, Optical transfer function $H(k_x)$ for *p* polarization at $\lambda_0 = 1{,}120$ nm, and the quadratic fitting in the form of $c_{pp}k_x^2$. **e**, Schematic of the simulation model for the bound-state-in-the-continuum (BIC) and quasi-guided modes. **f**, Top views of the E_z field profiles showing excitation of the BIC (top) and quasi-guided mode (bottom) at $k_x = 0$ and $0.12(2\pi/a)$, respectively. The symmetry plane is denoted by the yellow dashed line ($y = 0$). **g**, Side views of the E_z field distributions for the BIC ($k_x = 0$, left) and quasi-guided mode at $k_x = 0.12$ ($2\pi/a$, right).

with an NA that is large enough for integration into both traditional and non-traditional imaging systems, allowing for compact optical analog image-processing systems.

To realize the required transfer function we used a 2D photonic crystal composed of cylindrical Si nanorods embedded in polymethyl methacrylate (PMMA) on a silicon dioxide (SiO_2) substrate (Fig. 1a,b). The nanorods have a height of 440 nm, diameter of 280 nm and period of 600 nm. Figure 1c shows the simulated colour-coded transmission coefficient amplitude $|t(f,\theta)|$ as a function of frequency and incident angle (θ_{air}) along the Γ–X direction ($\varphi = 0°$, where φ is the azimuthal angle in the horizontal plane) for *s* and *p* polarization. It is worth noting that no polarization conversions occurs for the transmitted light. At normal incidence, two broad transmission dips are observed at 244 and 268 THz, indicating the presence of two Mie resonances with low quality factor. There is also a bound state in the continuum (BIC) at 249 THz, which is completely decoupled from free space at the Γ point due to symmetry protection[27,28]. At oblique incidence, the transmission follows a different trend for *s* and *p* polarization. Under *s* polarization, the dipole resonant frequencies remain unchanged as a function of incident angle. The invariant resonance results in no transmitted light for *s*-polarized input (transmission spectra at other angles φ are provided in Supplementary Fig. 2). Due to the mirror symmetry of the photonic crystal with respect to the horizontal plane ($z = 0$), regardless of the incident polarization, there is also no *s*-polarized output based on optical reciprocity, leading to the matrix components c_{ss}, c_{sp} and c_{ps} being zero in equation (1). However, under *p* polarization, the BIC resonance begins to couple to free space, becoming quasi-guided with a finite lifetime, and a Fano resonance results in a rapid change in transmittance as the incident angle becomes larger (additional details regarding the response are provided in Supplementary Section 1 and Supplementary Fig. 3). We chose the working frequency of 268 THz ($\lambda_0 = 1{,}120$ nm), away from the BIC, to obtain the proper transfer function. The resulting modulation transfer function $|H(k_x)|$ and phase along the Γ–X direction for *p* polarization are shown in Fig. 1d. Importantly, the modulation transfer function has the required quadratic dependence given by $H(k_x) = c_{pp}k_x^2$, shown by a fit to the simulated data. The quadratic curve is a near perfect fit up to an NA (nk_x) = 0.315, which equates to an edge resolution on the scale of 2.17 μm (1.94λ). To balance the roles of NA, accuracy of the transfer function and transmittance for image differentiation, we define the differentiation efficiency η as the square of the transfer function ($|H(k)|^2$) at the maximum spatial frequencies that can be fitted to the desirable mathematical function (the Laplacian for this work). In this regard, the efficiency can be as high as 81% at an NA = 0.315. Because the maximum NA also depends on the fitting accuracy, we can also expand the maximum fitted NA to 0.326 to achieve an efficiency of 90%, at a slight expense to the accuracy (for details of the fitting and a summary of previous works see Supplementary Table 1 and Supplementary Fig. 1).

To better understand the polarization dependence, we examined the profile of the BIC mode as a function of in-plane wavevector. The structure was modelled using a finite-difference time-domain (FDTD) solver (MEEP[29]) by placing an electric dipole, E_z (red dot, Fig. 1e), within the slab at the BIC frequency of 249 THz, then the in-plane wavevector was swept long the Γ–X direction, as shown in Fig. 1e (for details of the simulation see Methods). Top view of the E_z field profiles are shown in Fig. 1f, showing the excitation of a

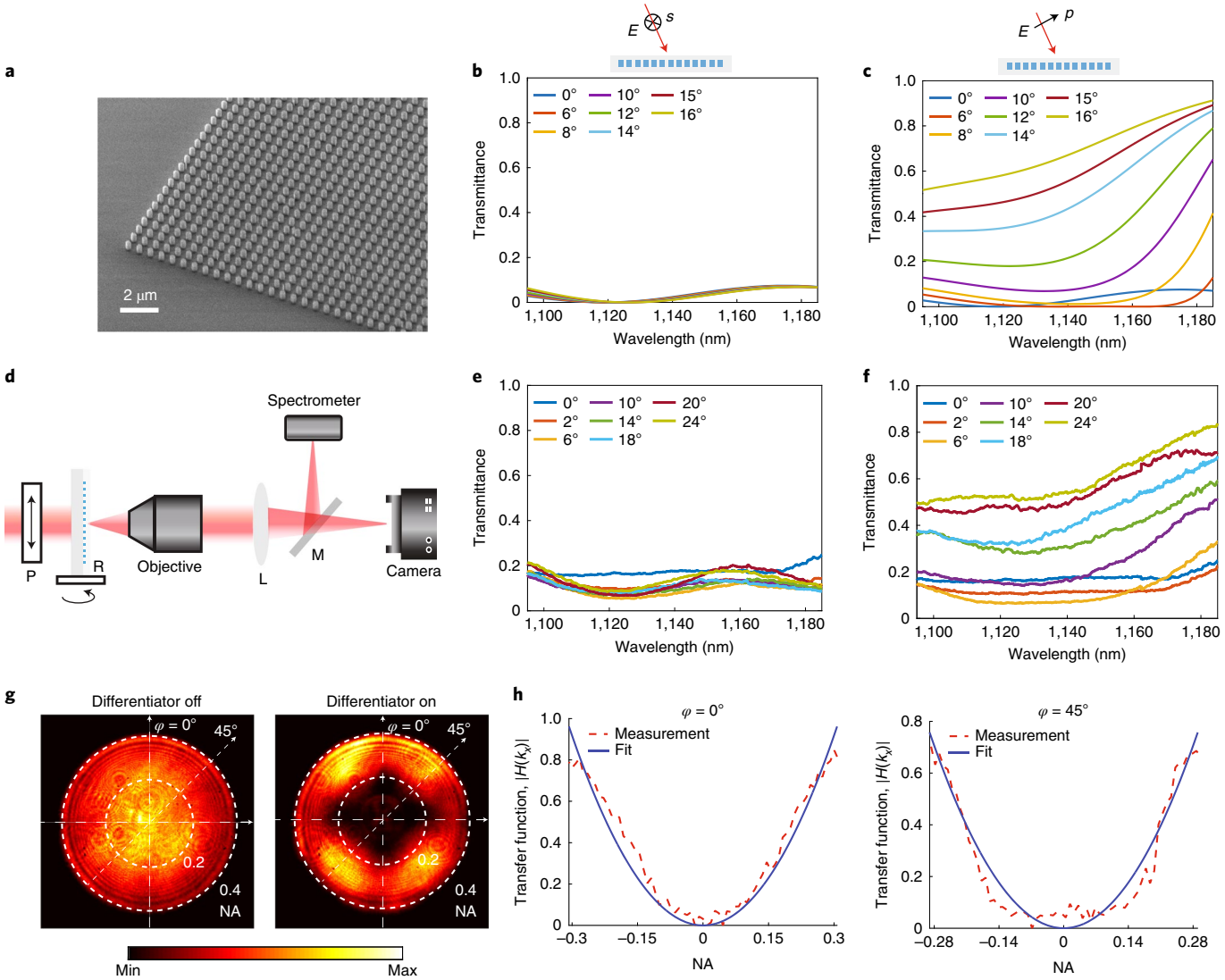

Fig. 2 | Fabrication and characterization of the nanophotonic spatial differentiator. a, SEM image of the fabricated Si photonic crystal. **b**,**c**, Simulated transmission spectra along the Γ–X direction for *s* (**b**) and *p* (**c**) polarization. **d**, Experimental set-up for measuring the transmission spectra at various angles. P, polarizer; R, rotation stage; L, tube lens ($f = 200$ mm); M, flip mirror. **e**,**f**, Measured transmission spectra for *s*-polarized (**e**) and *p*-polarized (**f**) incident light. **g**, Measured back focal plane images without and with the nanophotonic differentiator. **h**, Extracted 1D modulated transfer function along $\varphi = 0°$ and 45°.

vertical electric dipole. For a system with a sub-diffractional period, the array of dipoles oscillates in-phase, supporting in-plane radiation completely decoupled from free space. Away from the Γ point, this state starts to become quasi-guided and radiative as the symmetry is no longer protected, as can be seen from the side views of the E_z field distributions in Fig. 1g. Along the Γ–X direction, odd and even modes with respect to the vertical mirror plane ($y = 0$) can be excited by the *s* and *p* components, respectively. Based on symmetry considerations, the photonic crystal slab only couples to free-space modes of the same type of symmetry[27,30]. Thus, the quasi-guided mode, which possess an even symmetry (Fig. 1f), can only be excited by *p* polarization, leading to an angularly dependent transmission for *p* polarization while remaining reflective for *s* polarization. Additional details regarding the theoretical analysis are provided in Supplementary Section 1 and Supplementary Fig. 3.

To experimentally validate the design, we fabricated a 200 × 200 μm² differentiator using electron-beam lithography (EBL) in conjunction with reactive ion etching (RIE). A scanning electron microscopy (SEM) image of the fabricated device is shown in Fig. 2a. The simulated transmission spectra are presented in Fig. 2b,c for *s* and *p* polarization, respectively, and a schematic of the measurement set-up is shown in Fig. 2d. To acquire angle-dependent transmission measurements, the sample was mounted on a rotation stage and imaged through a magnification system composed of an objective paired with a tube lens. Figure 2e,f shows the measured transmission spectra at various incident angles under *s* and *p* polarization, respectively. The incident light is along the Γ–X direction with angles ranging from 0° to 24°. The trend and shape of the measured spectra are in good agreement with the simulation. To map the entire transfer function in *k*-space, we carried out Fourier plane imaging of the device. The nanophotonic differentiator was illuminated by unpolarized light at a wavelength of 1,120 nm and a ×50 objective (NA = 0.42) was used as a condenser with the Fourier images acquired in the back focal plane of a ×20 objective (NA = 0.4). Figure 2g,h shows the measured back focal plane imaging and the transfer function $|H(k)|$ along the $\varphi = 0°$ (Γ–X) and $\varphi = 45°$ azimuthal plane (Γ–M). Along the Γ–X direction, the transfer function matches with the fitted parabolic curve over an

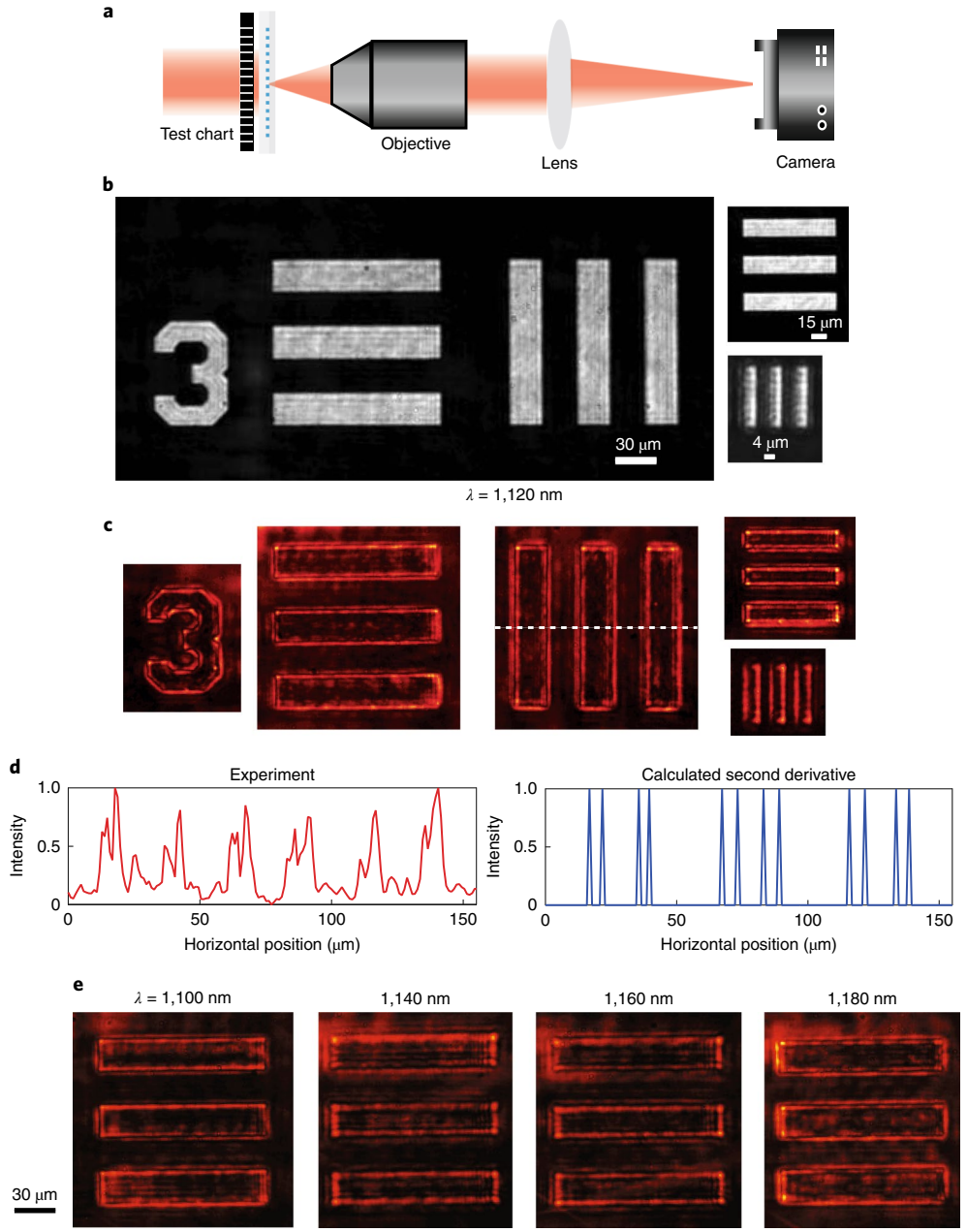

Fig. 3 | Differentiator resolution characterization. a, A schematic of the imaging set-up. The nanophotonic differentiator is placed directly in front of a standard 1951 USAF test chart and the targets are magnified through an objective paired with a tube lens. **b**,**c**, Imaging results for the target without (**b**) and with (**c**) the differentiator. **d**, Horizontal cut through the image in **c** (white dashed line), compared to the calculated second-order derivative calculated by the Laplacian of Gaussian filter. **e**, Edge detection results at different wavelengths ranging from $\lambda_0 = 1{,}100$ nm to 1,180 nm.

NA = 0.305. Although the Fourier imaging indicates a non-isotropic transfer function, the Laplacian transform at $\varphi = 45°$ can still be fitted with a quadratic function up to an NA = 0.28.

To experimentally quantify the resolution, we used the nanophotonic differentiator to detect the edges of a 1951 USAF resolution test chart. A schematic of the imaging set-up is shown in Fig. 3a. The test chart was illuminated using unpolarized and collimated light with a wavelength of 1,120 nm. Unlike previous experimental work[16,18], in this case no polarizers are needed to implement image differentiation, which further reduces the system footprint and complexity. The differentiator was placed directly in front of the test chart, which was then imaged through a magnification system comprising an objective paired with a tube lens and a near-infrared camera. The imaging results without the differentiator for element sizes ranging from 30 μm to 4 μm are shown in Fig. 3b. Figure 3c shows the images of the test chart after being passed through the differentiator. The edges of the micrometre-scale elements are clearly revealed along both horizontal and vertical directions, which indicates 2D spatial differentiation with a resolution smaller than 4 μm. Figure 3d shows the horizontal-cut intensity distributions through the differentiated images in Fig. 3c (white dashed line), compared to the second-order derivative based on the Laplacian of Gaussian filter. Due to the nature of the second-order derivative, two closely spaced peaks are formed around each edge, which can be observed from both the calculation and measurement. It is also important to note that the differentiator can operate over a relatively broad band

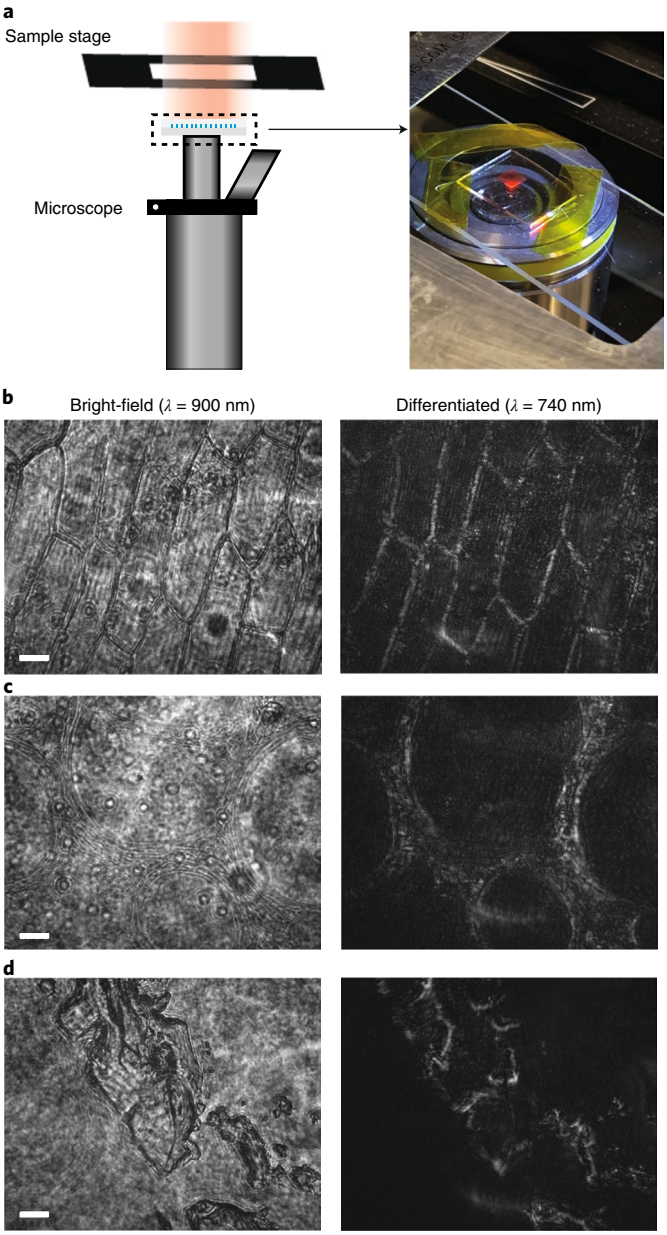

Fig. 4 | Edge detection microscope at visible frequencies. a, Schematic of the edge detection microscope. The spatial differentiator is redesigned at a wavelength of $\lambda_0 = 740$ nm and fabricated with dimensions of 3.5×3.5 mm^2, which is directly integrated with a commercial inverted optical microscope (Axio Vert.A1). **b**–**d**, Imaging and edge detection results for three types of biological cell sample: onion epidermis (**b**), pumpkin stem (**c**) and pig motor nerve (**d**). Images on the left are obtained at a wavelength of $\lambda = 900$ nm, which is away from the resonant frequency, and the images on the right correspond to the results at the working wavelength of $\lambda_0 = 740$ nm. Scale bars, 50 μm.

due to the low quality factor resonance away from the BIC state (for details of modulation transfer functions at other wavelengths see Supplementary Fig. 4). Although the differentiator is not an ideal Laplacian operator away from the designed wavelength, the images in Fig. 3e indicate that it can still be used for edge discrimination across a bandwidth from 1,100 and 1,180 nm.

One of the primary benefits of flat optics is the ability to vertically integrate them with traditional optical systems. To demonstrate the potential of this approach, we built an edge detection microscope by integrating the image differentiator with a commercial optical microscope (Zeiss Axio Vert.A1). In this case, the nanophotonic differentiator was redesigned for a wavelength of 740 nm using pillars with a diameter of 180 nm, a period of 385 nm and a height of 280 nm. Figure 4a presents a schematic of the microscope set-up. The differentiator has dimensions of 3.5×3.5 mm^2 and is placed below the sample stage directly on top of the microscope objective (×10). An unpolarized monochromatic laser ($\lambda_0 = 740$ nm) was used as the light source incident from the top and imaged on a charge-coupled device (CCD; uEye). Three types of biological cell were used as the imaging specimen. Figure 4b–d shows the imaging and edge detection results of onion epidermis (Fig. 4b), pumpkin stem (Fig. 4c) and pig motor nerve (Fig. 4d). The bright-field images were obtained at a wavelength of $\lambda = 900$ nm, which is away from the quasi-guided resonance. It can be seen that the shapes and boundaries of cells are less discernible due to the transparent nature of the specimen. By switching to the working wavelength of $\lambda_0 = 740$ nm, we observe clear and high-contrast cell boundaries (shown on the right). Here, the size of the differentiator is on the same order, but slightly smaller, than the objective's aperture. This could result in the differentiator acting as a beam block, allowing light at large wavevectors to pass around the edges. To exclude such an effect, a control device was made by placing a field stop around the differentiator while also placing the differentiator close to the cell sample. The results, shown in Supplementary Fig. 5, show that high-contrast cell boundaries are preserved, verifying that the edge enhancement is due to the transfer function of the differentiator. This edge enhancement is similar to dark-field microscopy but without the use of complex components such as a condenser annulus, which has to be aligned in the optical pathway, resulting in significantly reduced system complexity.

Another way in which the differentiator can be used in traditional optical systems is by integration onto a camera sensor. In this case, and in most practical computer vision applications, fabrication at much larger scales is necessary. One potential avenue for scale-up is to employ self-assembly-based nanosphere lithography, which takes advantage of the inherent periodicity and cylindrical unit cell geometry employed here. We have recently employed this method for realizing large-area reflectors and Fig. 5a shows a schematic flowchart of this fabrication process[31]. To investigate the feasibility of this technique for realizing the differentiator, we redesigned the device for an operational wavelength of 1,450 nm, which corresponds to a rod diameter of 340 nm, height of 480 nm and a hexagonal lattice with a period of 740 nm. This redesign was necessary to match the periodicity with the size of commercially available nanospheres. The fabrication technique, outlined in detail in the Methods, involves using an array of self-assembled nanospheres as an etch mask for the photonic crystal. Figure 5b presents an optical image of a fabricated ~1 cm × 1 cm image differentiator. The colour variation corresponds to different grain orientations, which does not affect the transmission at different incident angles (for details of the transmission map see Supplementary Fig. 6). The SEM images in Fig. 5c show high-quality Si resonators and a well-defined hexagonal lattice over a large area (Supplementary Fig. 7).

To mimic a configuration that may be found in a computer vision application, the large-scale spatial differentiator was placed directly in front of a NIR camera detector, after the imaging lens, as shown in Fig. 5d. For imaging targets we used transparent centimetre-sized plastic flower moulds (Fig. 5e,g) due to their curved surfaces, which scatter light at large angles. Figure 5f,h shows the imaging results with and without the differentiator for two separate objects. Compared to the bright-field images, the edges of the flowers are clearly revealed when applying the differentiator. Although we have not placed the differentiator directly on the

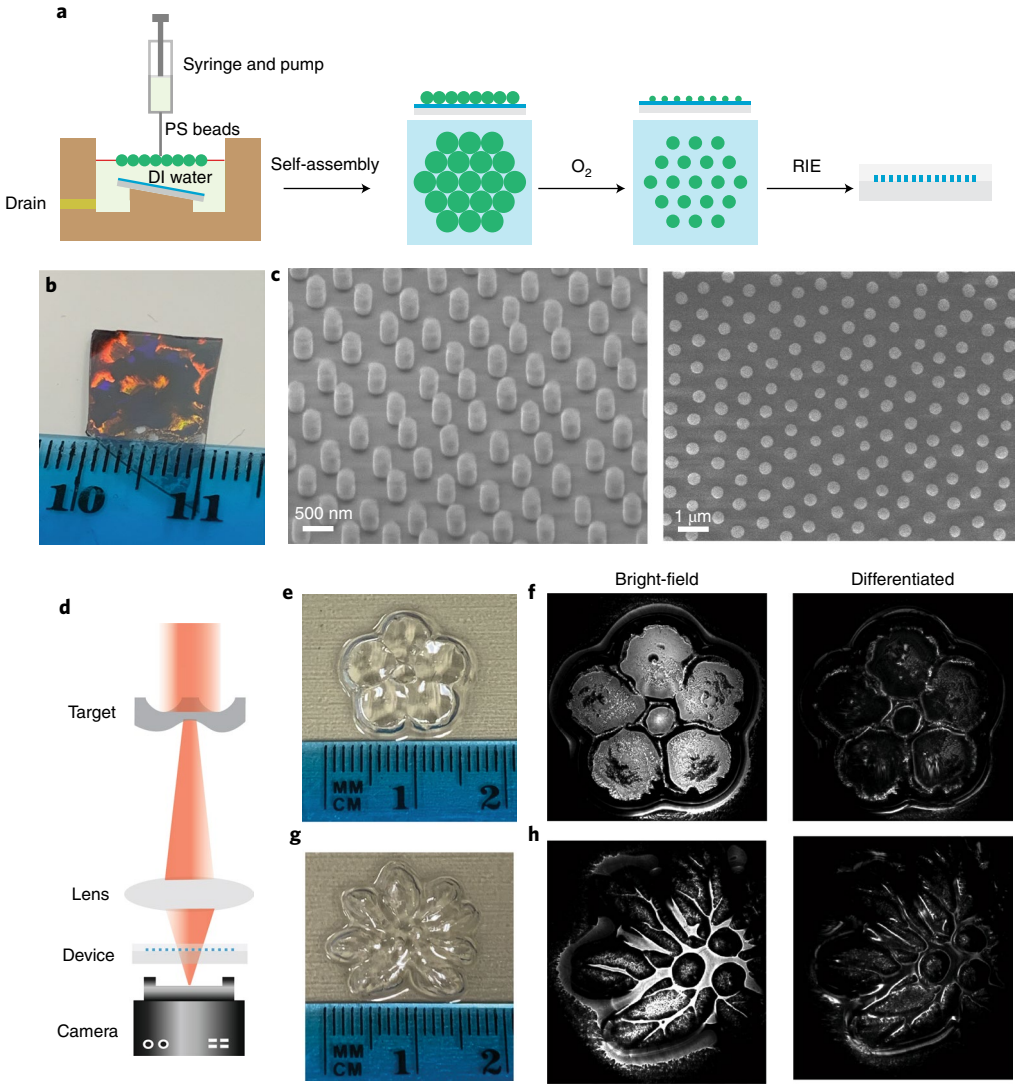

Fig. 5 | Large-scale image differentiator using nanosphere lithography. a, Flowchart of the fabrication process. A monolayer of nanospheres was formed at the water/air interface of a bath and then transferred to a tilted substrate with a Si film, resulting in densely packed nanospheres arranged in a hexagonal lattice. The nanospheres were then downsized and used as a dry etch mask for defining the Si nanostructures. PS, polystyrene; DI water, deionized water. **b**, Optical image of a centimetre-scale differentiator. **c**, SEM images of the Si rods. **d**, Schematic of the imaging set-up. The large-scale device is placed in front of a near-infrared (NIR) camera sensor. **e**, Optical image of a plastic flower mould, which was used as a 3D macroscopic imaging target. **f**, Bright-field and differentiated results for the same target. Images on the left and right correspond to systems without and with the differentiator, respectively. **g**,**h**, The same imaging results as in **e** and **f**, on a second target.

sensor in this case, there is nothing that would prevent this level of integration in creating a monolithic edge-detecting sensor for computer vision applications.

Finally, although we have showcased vertical integration with convention optics, the imaging system can be further compacted by employing a metalens as the focusing element for realizing an ultrathin and monolithic image-processing system. To create such a device we used multilayer metasurface transfer techniques, which we have employed previously for creating doublet lenses[32] and other multilayer metaoptics[33]. Briefly, the metalens and differentiator were designed for operation at $\lambda = 1{,}120$ nm and fabricated on separate wafers (with dimensions of $\sim 2 \times 2\,\mathrm{mm}^2$), followed by embedding the structures in polydimethylsiloxane. The differentiator layer was then released from the handle wafer and transferred on top of the metalens. Figure 6a,b are optical images of the released differentiator and metalens, respectively, which were combined to form the compound monolithic element shown in Fig. 6c (additional details regarding the fabrication are provided in Supplementary Section 3 and Supplementary Fig. 8). The compound metaoptic was then used as an ultrathin system to image a micrometre-scale target (Fig. 6d). Figure 6e shows the bright-field and differentiated images of onion cells for wavelengths of 1,280 and 1,120 nm, respectively. At the off-resonant wavelength ($\lambda = 1{,}280$ nm) the images are formed without differentiation, while at resonance ($\lambda = 1{,}120$ nm) there is significant edge enhancement for each of the cell walls. In this case there is more noise in the images compared to the experiments employing the differentiator on an objective lens or camera sensor. We believe that the additional noise can be attributed to the diffractive artefacts from the metalens due to non-unity focusing efficiency, an issue that is slightly exaggerated due to the weaker signal strength after passing through the differentiator. This issue can be minimized by optimizing the lens design[34,35] and fabrication[36,37].

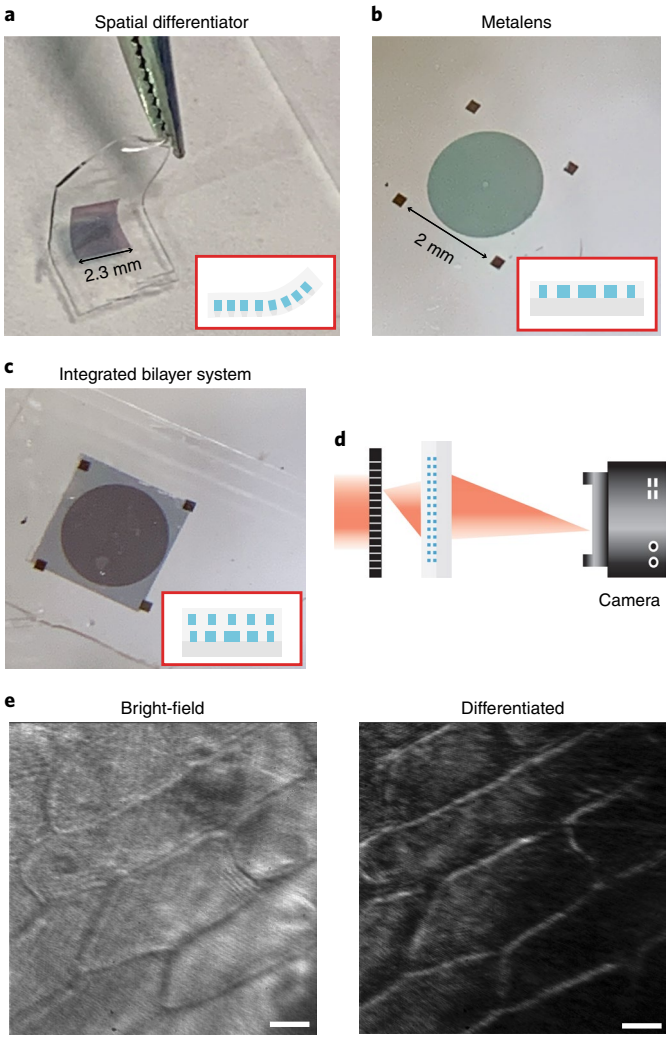

Fig. 6 | Compound metaoptic. a–c, Optical images of the nanophotonic differentiator (**a**), metalens (**b**) and monolithic compound system (**c**). The insets show schematics of the device cross-sections. **d**, Schematic of the imaging set-up. **e**, Imaging results for bright-field (left) and differentiated (right) onion cells. Scale bars, 50 μm.

Discussion

In conclusion, we have experimentally demonstrated 2D image differentiators with high resolution, thin form factor and a simple geometry that allows rapid and cost-effective large-scale manufacturing. Furthermore, we have demonstrated how a complete image-processing system can be accomplished using monolithic compound flat optics. These types of optical analog image processors could open new doors for applications in areas such as biological imaging and computer vision. Metaoptics with a more complex *k*-space response could also be realized by employing multilayer architectures[32,33] and inverse design[35,38,39] for more complex optical analog computing and image filtering.

Online content

Any methods, additional references, Nature Research reporting summaries, source data, extended data, supplementary information, acknowledgements, peer review information; details of author contributions and competing interests; and statements of data and code availability are available at https://doi.org/10.1038/s41566-020-0591-3.

Received: 11 September 2019; Accepted: 15 January 2020;
Published online: 24 February 2020

References

1. Marr, D. & Hildreth, E. Theory of edge detection. *Proc. R. Soc. Lond. B* **207**, 187–217 (1980).
2. Canny, J. A computational approach to edge detection. *IEEE Trans. Pattern Anal. Mach. Intell.* **8**, 679–698 (1986).
3. Hsu, H.-S. & Tsai, W.-H. Moment-preserving edge detection and its application to image data compression. *Opt. Eng.* **32**, 1596 (1993).
4. Brosnan, T. & Sun, D.-W. Improving quality inspection of food products by computer vision—a review. *J. Food Eng.* **61**, 3–16 (2004).
5. Fürhapter, S., Jesacher, A., Bernet, S. & Ritsch-Marte, M. Spiral phase contrast imaging in microscopy. *Opt. Express* **13**, 689–694 (2005).
6. Gebäck, T. & Koumoutsakos, P. Edge detection in microscopy images using curvelets. *BMC Bioinformatics* **10**, 75 (2009).
7. Cardullo, R. A. Fundamentals of image processing in light microscopy. *Methods Cell Biol.* **72**, 217–242 (2003).
8. Haralick, R. M. & Shapiro, L. G. Computer and robot vision. *IEEE Robot. Autom. Mag.* **1**, 28–48 (1991).
9. Solli, D. R. & Jalali, B. Analog optical computing. *Nat. Photon.* **9**, 704–706 (2015).
10. Yu, N. & Capasso, F. Flat optics with designer metasurfaces. *Nat. Mater.* **13**, 139–150 (2014).
11. Joannopoulos, J. D., Villeneuve, P. R. & Fan, S. Photonic crystals putting a new twist on light. *Nature* **386**, 143–149 (1997).
12. Silva, A. et al. Performing mathematical operations with metamaterials. *Science* **343**, 160–163 (2014).
13. Kwon, H., Sounas, D., Cordaro, A., Polman, A. & Alù, A. Nonlocal metasurfaces for optical signal processing. *Phys. Rev. Lett.* **121**, 173004 (2018).
14. Bykov, D. A., Doskolovich, L. L., Bezus, E. A. & Soifer, V. A. Optical computation of the Laplace operator using phase-shifted Bragg grating. *Opt. Express* **22**, 25084–25092 (2014).
15. Guo, C., Xiao, M., Minkov, M., Shi, Y. & Fan, S. Photonic crystal slab Laplace operator for image differentiation. *Optica* **5**, 251 (2018).
16. Cordaro, A. et al. High-index dielectric metasurfaces performing mathematical operations. *Nano Lett.* **19**, 8418–8423 (2019).
17. Zhu, T. et al. Generalized spatial differentiation from the spin Hall effect of light and its application in image processing of edge detection. *Phys. Rev. Appl.* **11**, 034043 (2019).
18. Zhu, T. et al. Plasmonic computing of spatial differentiation. *Nat. Commun.* **8**, 15391 (2017).
19. Zhou, J. et al. Optical edge detection based on high-efficiency dielectric metasurface. *Proc. Natl Acad. Sci. USA* **116**, 11137–11140 (2019).
20. Bracewell, R. N. *The Fourier Transform and its Applications* (McGraw Hill, 2000).
21. Krivenkov, V. I. Guided modes in photonic crystal fibers. *Dokl. Phys.* **48**, 414–417 (2003).
22. Fan, S. & Joannopoulos, J. D. Analysis of guided resonances in photonic crystal slabs. *Phys. Rev. B* **65**, 235112 (2002).
23. Zhou, W. et al. Progress in 2D photonic crystal Fano resonance photonics. *Prog. Quantum Electron.* **38**, 1–74 (2014).
24. Liu, Z. S., Tibuleac, S., Shin, D., Young, P. P. & Magnusson, R. High-efficiency guided-mode resonance filter. *Opt. Lett.* **23**, 1556–1558 (1998).
25. Suh, W., Yanik, M. F., Solgaard, O. & Fan, S. Displacement-sensitive photonic crystal structures based on guided resonance in photonic crystal slabs. *Appl. Phys. Lett.* **82**, 1999–2001 (2003).
26. Winn, J. N., Fink, Y., Fan, S. & Joannopoulos, J. D. Omnidirectional reflection from a one-dimensional photonic crystal. *Opt. Lett.* **23**, 1573–1575 (1998).
27. Hsu, C. W., Zhen, B., Stone, A. D., Joannopoulos, J. D. & Soljacic, M. Bound states in the continuum. *Nat. Rev. Mater* **1**, 16048 (2016).
28. Xu, L. et al. Dynamic nonlinear image tuning through magnetic dipole quasi-BIC ultrathin resonators. *Adv. Sci.* **6**, 1802119 (2019).
29. Oskooi, A. F. et al. Meep: a flexible free-software package for electromagnetic simulations by the FDTD method. *Comput. Phys. Commun.* **181**, 687–702 (2010).
30. Lee, J. et al. Observation and differentiation of unique high-*Q* optical resonances near zero wave vector in macroscopic photonic crystal slabs. *Phys. Rev. Lett.* **109**, 067401 (2012).
31. Moitra, P. et al. Large-scale all-dielectric metamaterial perfect reflectors. *ACS Photon.* **2**, 692–698 (2015).
32. Zhou, Y. et al. Multilayer noninteracting dielectric metasurfaces for multiwavelength metaoptics. *Nano Lett.* **18**, 7529–7537 (2018).
33. Zhou, Y. et al. Multifunctional metaoptics based on bilayer metasurfaces. *Light Sci. Appl.* **8**, 80 (2019).

34. Phan, T. et al. High-efficiency, large-area, topology-optimized metasurfaces. *Light Sci. Appl.* **8**, 48 (2019).
35. Molesky, S. et al. Outlook for inverse design in nanophotonics. *Nat. Photon.* **12**, 659–670 (2018).
36. Arbabi, A., Horie, Y., Ball, A. J., Bagheri, M. & Faraon, A. Subwavelength-thick lenses with high numerical apertures and large efficiency based on high-contrast transmitarrays. *Nat. Commun.* **6**, 7069 (2015).
37. Khorasaninejad, M. et al. Metalenses at visible wavelengths: diffraction-limited focusing and subwavelength resolution imaging. *Science* **352**, 1190–1194 (2016).
38. Lin, Z., Groever, B., Capasso, F., Rodriguez, A. W. & Lončar, M. Topology-optimized multilayered metaoptics. *Phys. Rev. Appl.* **9**, 044030 (2018).
39. Sell, D., Yang, J., Doshay, S., Yang, R. & Fan, J. A. Large-angle, multifunctional metagratings based on freeform multimode geometries. *Nano Lett.* **17**, 3752–3757 (2017).

Methods

Simulations. The transmission spectra were calculated using the frequency domain solver of CST Microwave Studio. The refractive index of SiO_2 and PMMA were set to 1.45 and 1.48, respectively, and the index of Si (3.67 at 1,120 nm) was obtained using ellipsometry. The Si nanorods were modelled as a periodic unit cell on a SiO_2 substrate embedded in a PMMA cladding layer.

Simulations of the BIC and quasi-guided modes in Fig. 1e–g were carried out using an open-source FDTD solver (Meep[29]). The Si nanorod array was modelled as a unit cell embedded in a uniform background ($n = 1.45$). Perfectly matched layers were added at the top and bottom as the boundaries along the z direction. An electric dipole source, E_z, was placed within the slab at a frequency of 249 THz and the in-plane wavevector was swept long the Γ–X direction to excite the structure at $k_x = 0$ and $0.12(2\pi/a)$, respectively.

Fabrication. The photonic crystal slab was defined in a 440 nm-thick amorphous Si layer that was grown on a SiO_2 substrate using low-pressure chemical vapour deposition (LPCVD). A 200 nm PMMA 950K A4 layer was spin-coated at 4,500 r.p.m. followed by deposition of 10 nm-thick chromium as the conduction layer using thermal evaporation. The patterns were then defined using EBL followed by depositing 35 nm-thick alumina oxide as a dry etch mask using electron-beam evaporation. The Si nanorods were etched using RIE using a mixture of C_4F_8 and SF_6, Finally, five layers of PMMA A4 were sequentially spin-coated to encapsulate the Si nanorods. The same procedure was also used for fabricating the visible image differentiator.

In the case of nanosphere lithography, a monolayer of 740 nm-diameter nanospheres was first formed at the water/air interface of a bath through controlled injection by a syringe pump. A wafer with a 480 nm-thick layer of Si on SiO_2 was tilted at 10° and placed at the bottom of the Teflon bath. The densely packed hexagonal nanospheres were transferred to the wafer by slowly draining the bath. The nanospheres were then downscaled using an O_2 plasma and used as an etch mask during RIE to define the Si rods. The fabrication details for the compound metaoptics and additional details regarding nanosphere lithography are provided in Supplementary Sections 2 and 3.

Data availability

The data that support the plots within this paper and other findings of this study are available from the corresponding author upon reasonable request.

Acknowledgements

We acknowledge support from the Office of Naval Research under award no. N00014-18-1-2563 and DARPA under the NLM programme, award no. HR001118C0015. Part of the fabrication process was conducted at the Center for Nanophase Materials Sciences, which is a DOE Office of Science User Facility. The remainder of the fabrication process took place in the Vanderbilt Institute of Nanoscale Science and Engineering (VINSE) and we thank the staff, particularly K. Heinrich, for their support.

Author contributions

Y.Z. and J.V. developed the idea. Y.Z. conducted the modelling and theoretical analysis. Y.Z. and H.Z. fabricated the samples with small die size (less than 1 mm^2) and H.Z. fabricated the samples based on self-assembled masks. I.I.K. provided the substrates and fabricated the larger die size samples not based on self-assembled masks. Y.Z. performed all of the experimental measurements and data analysis, with assistance from H.Z. Y.Z. and J.V. wrote the manuscript with input from all of the authors. The project was supervised by J.V.

Competing interests

Y.Z., H.Z. and J.V. have submitted a patent application for this work, assigned to Vanderbilt University.

Additional information

Supplementary information is available for this paper at https://doi.org/10.1038/s41566-020-0591-3.

Correspondence and requests for materials should be addressed to J.V.